Photon and neutral pion production in Au+Au collisions at $\sqrt{s_{NN}}$=130 GeV

J. Adams,[3] C. Adler,[12] M. M. Aggarwal,[25] Z. Ahammed,[28] J. Amonett,[17] B. D. Anderson,[17] M. Anderson,[5] D. Arkhipkin,[11] G. S. Averichev,[10] S. K. Badyal,[16] J. Balewski,[13] O. Barannikova,[28,10] L. S. Barnby,[17] J. Baudot,[15] S. Bekele,[24] V. V. Belaga,[10] R. Bellwied,[41] J. Berger,[12] B. I. Bezverkhny,[43] S. Bhardwaj,[29] P. Bhaskar,[38] A. K. Bhati,[25] H. Bichsel,[40] A. Billmeier,[41] L. C. Bland,[2] C. O. Blyth,[3] B. E. Bonner,[30] M. Botje,[23] A. Boucham,[34] A. Brandin,[21] A. Bravar,[2] R. V. Cadman,[1] X. Z. Cai,[33] H. Caines,[43] M. Calderón de la Barca Sánchez,[2] J. Carroll,[18] J. Castillo,[18] M. Castro,[41] D. Cebra,[5] P. Chaloupka,[9] S. Chattopadhyay,[38] H. F. Chen,[32] Y. Chen,[6] S. P. Chernenko,[10] M. Cherney,[8] A. Chikanian,[43] B. Choi,[36] W. Christie,[2] J. P. Coffin,[15] T. M. Cormier,[41] J. G. Cramer,[40] H. J. Crawford,[4] D. Das,[38] S. Das,[38] A. A. Derevschikov,[27] L. Didenko,[2] T. Dietel,[12] X. Dong,[32,18] J. E. Draper,[5] F. Du,[43] A. K. Dubey,[14] V. B. Dunin,[10] J. C. Dunlop,[2] M. R. Dutta Majumdar,[38] V. Eckardt,[19] L. G. Efimov,[10] V. Emelianov,[21] J. Engelage,[4] G. Eppley,[30] B. Erazmus,[34] M. Estienne,[34] P. Fachini,[2] V. Faine,[2] J. Faivre,[15] R. Fatemi,[13] K. Filimonov,[18] P. Filip,[9] E. Finch,[43] Y. Fisyak,[2] D. Flierl,[12] K. J. Foley,[2] J. Fu,[42] C. A. Gagliardi,[35] M. S. Ganti,[38] T. D. Gutierrez,[5] N. Gagunashvili,[10] J. Gans,[43] L. Gaudichet,[34] M. Germain,[15] F. Geurts,[30] V. Ghazikhanian,[6] P. Ghosh,[38] J. E. Gonzalez,[6] O. Grachov,[41] V. Grigoriev,[21] S. Gronstal,[8] D. Grosnick,[37] M. Guedon,[15] S. M. Guertin,[6] A. Gupta,[16] E. Gushin,[21] T. J. Hallman,[2] D. Hardtke,[18] J. W. Harris,[43] M. Heinz,[43] T. W. Henry,[35] S. Heppelmann,[26] T. Herston,[28] B. Hippolyte,[43] A. Hirsch,[28] E. Hjort,[18] G. W. Hoffmann,[36] M. Horsley,[43] H. Z. Huang,[6] S. L. Huang,[32] T. J. Humanic,[24] G. Igo,[6] A. Ishihara,[36] P. Jacobs,[18] W. W. Jacobs,[13] M. Janik,[39] I. Johnson,[18] P. G. Jones,[3] E. G. Judd,[4] S. Kabana,[43] M. Kaneta,[18] M. Kaplan,[7] D. Keane,[17] J. Kiryluk,[6] A. Kisiel,[39] J. Klay,[18] S. R. Klein,[18] A. Klyachko,[13] D. D. Koetke,[37] T. Kollegger,[12] A. S. Konstantinov,[27] M. Kopytine,[17] L. Kotchenda,[21] A. D. Kovalenko,[10] M. Kramer,[22] P. Kravtsov,[21] K. Krueger,[1] C. Kuhn,[15] A. I. Kulikov,[10] A. Kumar,[25] G. J. Kunde,[43] C. L. Kunz,[7] R. Kh. Kutuev,[11] A. A. Kuznetsov,[10] M. A. C. Lamont,[3] J. M. Landgraf,[2] S. Lange,[12] C. P. Lansdell,[36] B. Lasiuk,[43] F. Laue,[2] J. Lauret,[2] A. Lebedev,[2] R. Lednický,[10] V. M. Leontiev,[27] M. J. LeVine,[2] C. Li,[32] Q. Li,[41] S. J. Lindenbaum,[22] M. A. Lisa,[24] F. Liu,[42] L. Liu,[42] Z. Liu,[42] Q. J. Liu,[40] T. Ljubicic,[2] W. J. Llope,[30] H. Long,[6] R. S. Longacre,[2] M. Lopez-Noriega,[24] W. A. Love,[2] T. Ludlam,[2] D. Lynn,[2] J. Ma,[6] Y. G. Ma,[33] D. Magestro,[24] S. Mahajan,[16] L. K. Mangotra,[16] D. P. Mahapatra,[14] R. Majka,[43] R. Manweiler,[37] S. Margetis,[17] C. Markert,[43] L. Martin,[34] J. Marx,[18] H. S. Matis,[18] Yu. A. Matulenko,[27] T. S. McShane,[8] F. Meissner,[18] Yu. Melnick,[27] A. Meschanin,[27] M. Messer,[2] M. L. Miller,[43] Z. Milosevich,[7] N. G. Minaev,[27] C. Mironov,[17] D. Mishra,[14] J. Mitchell,[30] B. Mohanty,[38] L. Molnar,[28] C. F. Moore,[36] M. J. Mora-Corral,[19] V. Morozov,[18] M. M. de Moura,[41] M. G. Munhoz,[31] B. K. Nandi,[38] S. K. Nayak,[16] T. K. Nayak,[38] J. M. Nelson,[3] P. Nevski,[2] V. A. Nikitin,[11] L. V. Nogach,[27] B. Norman,[17] S. B. Nurushev,[27] G. Odyniec,[18] A. Ogawa,[2] V. Okorokov,[21] M. Oldenburg,[18] D. Olson,[18] G. Paic,[24] S. U. Pandey,[41] S. K. Pal,[38] Y. Panebratsev,[10] S. Y. Panitkin,[2] A. I. Pavlinov,[41] T. Pawlak,[39] V. Perevoztchikov,[2] W. Peryt,[39] V. A. Petrov,[11] S. C. Phatak,[14] R. Picha,[5] M. Planinic,[44] J. Pluta,[39] N. Porile,[28] J. Porter,[2] A. M. Poskanzer,[18] M. Potekhin,[2] E. Potrebenikova,[10] B. V. K. S. Potukuchi,[16] D. Prindle,[40] C. Pruneau,[41] J. Putschke,[19] G. Rai,[18] G. Rakness,[13] R. Raniwala,[29] S. Raniwala,[29] O. Ravel,[34] R. L. Ray,[36] S. V. Razin,[10,13] D. Reichhold,[28] J. G. Reid,[40] G. Renault,[34] F. Retiere,[18] A. Ridiger,[21] H. G. Ritter,[18] J. B. Roberts,[30] O. V. Rogachevski,[10] J. L. Romero,[5] A. Rose,[41] C. Roy,[34] L. J. Ruan,[32,2] R. Sahoo,[14] I. Sakrejda,[18] S. Salur,[43] J. Sandweiss,[43] I. Savin,[11] J. Schambach,[36] R. P. Scharenberg,[28] N. Schmitz,[19] L. S. Schroeder,[18] K. Schweda,[18] J. Seger,[8] D. Seliverstov,[21] P. Seyboth,[19] E. Shahaliev,[10] M. Shao,[32] M. Sharma,[25] K. E. Shestermanov,[27] S. S. Shimanskii,[10] R. N. Singaraju,[38] F. Simon,[19] G. Skoro,[10] N. Smirnov,[43] R. Snellings,[23] G. Sood,[25] P. Sorensen,[6] J. Sowinski,[13] H. M. Spinka,[1] B. Srivastava,[28] S. Stanislaus,[37] R. Stock,[12] A. Stolpovsky,[41] M. Strikhanov,[21] B. Stringfellow,[28] C. Struck,[12] A. A. P. Suaide,[41] E. Sugarbaker,[24] C. Suire,[2] M. Šumbera,[9] B. Surrow,[2] T. J. M. Symons,[18] A. Szanto de Toledo,[31] P. Szarwas,[39] A. Tai,[6] J. Takahashi,[31] A. H. Tang,[2,23] D. Thein,[6] J. H. Thomas,[18] V. Tikhomirov,[21] M. Tokarev,[10] M. B. Tonjes,[20] T. A. Trainor,[40] S. Trentalange,[6] R. E. Tribble,[35] M. D. Trivedi,[38] V. Trofimov,[21] O. Tsai,[6] T. Ullrich,[2] D. G. Underwood,[1] G. Van Buren,[2] A. M. VanderMolen,[20] A. N. Vasiliev,[27] M. Vasiliev,[35] S. E. Vigdor,[13] Y. P. Viyogi,[38] S. A. Voloshin,[41] W. Waggoner,[8] F. Wang,[28] G. Wang,[17] X. L. Wang,[32] Z. M. Wang,[32] H. Ward,[36] J. W. Watson,[17] R. Wells,[24] G. D. Westfall,[20] C. Whitten Jr.,[6] H. Wieman,[18] R. Willson,[24] S. W. Wissink,[13] R. Witt,[43] J. Wood,[6] J. Wu,[32] N. Xu,[18] Z. Xu,[2] Z. Z. Xu,[32] A. E. Yakutin,[27] E. Yamamoto,[18] J. Yang,[6] P. Yepes,[30] V. I. Yurevich,[10] Y. V. Zanevski,[10] I. Zborovský,[9] H. Zhang,[43,2] H. Y. Zhang,[17] W. M. Zhang,[17] Z. P. Zhang,[32] P. A. Żołnierczuk,[13] R. Zoulkarneev,[11] J. Zoulkarneeva,[11] and A. N. Zubarev[10]

[1]*Argonne National Laboratory, Argonne, Illinois 60439, USA*
[2]*Brookhaven National Laboratory, Upton, New York 11973, USA*
[3]*University of Birmingham, Birmingham, United Kingdom*
[4]*University of California, Berkeley, California 94720, USA*
[5]*University of California, Davis, California 95616, USA*
[6]*University of California, Los Angeles, California 90095, USA*
[7]*Carnegie Mellon University, Pittsburgh, Pennsylvania 15213, USA*
[8]*Creighton University, Omaha, Nebraska 68178, USA*
[9]*Nuclear Physics Institute AS CR, Řež/Prague, Czech Republic*
[10]*Laboratory for High Energy (JINR), Dubna, Russia*
[11]*Particle Physics Laboratory (JINR), Dubna, Russia*
[12]*University of Frankfurt, Frankfurt, Germany*

[13]*Indiana University, Bloomington, Indiana 47408, USA*
[14]*Insitute of Physics, Bhubaneswar 751005, India*
[15]*Institut de Recherches Subatomiques, Strasbourg, France*
[16]*University of Jammu, Jammu 180001, India*
[17]*Kent State University, Kent, Ohio 44242, USA*
[18]*Lawrence Berkeley National Laboratory, Berkeley, California 94720, USA*
[19]*Max-Planck-Institut für Physik, Munich, Germany*
[20]*Michigan State University, East Lansing, Michigan 48824, USA*
[21]*Moscow Engineering Physics Institute, Moscow, Russia*
[22]*City College of New York, New York City, New York 10031, USA*
[23]*NIKHEF, Amsterdam, The Netherlands*
[24]*Ohio State University, Columbus, Ohio 43210, USA*
[25]*Panjab University, Chandigarh 160014, India*
[26]*Pennsylvania State University, University Park, Pennsylvania 16802, USA*
[27]*Institute of High Energy Physics, Protvino, Russia*
[28]*Purdue University, West Lafayette, Indiana 47907, USA*
[29]*University of Rajasthan, Jaipur 302004, India*
[30]*Rice University, Houston, Texas 77251, USA*
[31]*Universidade de Sao Paulo, Sao Paulo, Brazil*
[32]*University of Science and Technology of China, Anhui 230027, People's Republic of China*
[33]*Shanghai Institute of Nuclear Research, Shanghai 201800, People's Republic of China*
[34]*SUBATECH, Nantes, France*
[35]*Texas A&M, College Station, Texas 77843, USA*
[36]*University of Texas, Austin, Texas 78712, USA*
[37]*Valparaiso University, Valparaiso, Indiana 46383, USA*
[38]*Variable Energy Cyclotron Centre, Kolkata 700064, India*
[39]*Warsaw University of Technology, Warsaw, Poland*
[40]*University of Washington, Seattle, Washington 98195, USA*
[41]*Wayne State University, Detroit, Michigan 48201, USA*
[42]*Institute of Particle Physics, CCNU (HZNU), Wuhan 430079, People's Republic of China*
[43]*Yale University, New Haven, Connecticut 06520, USA*
[44]*University of Zagreb, Zagreb, HR-10002, Croatia*

(Received 17 December 2003; published 11 October 2004)

We report inclusive photon measurements about midrapidity ($|y|<0.5$) from ^{197}Au+^{197}Au collisions at $\sqrt{s_{NN}}=130$ GeV at RHIC. Photon pair conversions were reconstructed from electron and positron tracks measured with the Time Projection Chamber (TPC) of the STAR experiment. With this method, an energy resolution of $\Delta E/E \approx 2\%$ at 0.5 GeV has been achieved. Reconstructed photons have also been used to measure the transverse momentum (p_t) spectra of π^0 mesons about midrapidity ($|y|<1$) via the $\pi^0 \rightarrow \gamma\gamma$ decay channel. The fractional contribution of the $\pi^0 \rightarrow \gamma\gamma$ decay to the inclusive photon spectrum decreases by $20\% \pm 5\%$ between $p_t=1.65$ GeV/c and $p_t=2.4$ GeV/c in the most central events, indicating that relative to $\pi^0 \rightarrow \gamma\gamma$ decay the contribution of other photon sources is substantially increasing.

DOI: 10.1103/PhysRevC.70.044902 PACS number(s): 25.75.Dw

I. INTRODUCTION

Relativistic heavy ion collisions provide the opportunity to excite matter into extreme conditions in the laboratory. Of the particles which emerge from these collisions, photons are considered to be one of the most valuable probes of the dynamics and properties of the resulting systems [1–5]. Unlike hadrons, which have large interaction cross sections in dense matter, photons only interact electromagnetically and consequently have a long mean free path. This path length is typically much larger than the transverse size of the matter created in nuclear collisions [6]. Therefore, with high probability, photons will escape from the system undisturbed, retaining information about the physical conditions under which they were created.

Photons are produced in all stages of heavy ion collisions [1,3,4,6–13], from the first instant when the quarks and gluons of the opposing nuclei interact, through to long lived electromagnetic decays of final state hadrons. The production rate of photons during various stages of the created system has been theoretically calculated for a variety of initial conditions and scenarios. It has been demonstrated that the emission rate from a hadron gas can be comparable to that expected from quark–gluon Compton and quark–antiquark annihilation processes in a net-baryon free system of deconfined quarks and gluons [6]. However, recent two-loop cal-

culations which include the quark bremsstrahlung process predict that photon production rates in quark matter exceed those indicated by former one-loop calculations that only account for the Compton and annihilation processes [11,12]. These calculations indicate "that the emissions from quark matter can outshine those from the hadronic matter" [12], and that near and above $p_t = 2$ GeV/c the contribution from hard scattered partons becomes more abundant than thermal photons from a hot hadronic gas at RHIC energy [13]. Theoretical calculations and predictions like these underscore the importance of measuring photon spectra across a wide range of p_t to investigate the matter created in heavy ion collisions. The measurements presented in this paper extend above and below the interesting region around $p_t = 2$ GeV/c.

Of all photon production mechanisms, late stage electromagnetic decays of hadrons are the dominant source. At CERN SPS energies, photons from π^0 and η decays account for ~97% [5] of the inclusive photon spectrum. The remaining 3% arises from a combination of other sources, including electromagnetic decays of other hadrons such as the ω, η', and Σ^0. For these particles, thermal models that describe hadron production must be used to estimate the yields since their production rates have not yet been measured in heavy ion collisions at these energies. Measurement of the $\eta' \to \rho\gamma$ and $\Sigma^0 \to \Lambda\gamma$ decays appear to be promising with the energy resolution afforded by the photon reconstruction technique described in this paper. By estimating or measuring the yields of such particles, their contribution to the single photon spectrum from electromagnetic decays can be calculated. However, the precision necessary to disentangle the rate of direct photon production from the rate of photons produced by electromagnetic decays is an experimental and theoretical challenge.

STAR has begun to address this challenge by measuring the spectra of both photons and π^0s. Photons were measured by reconstructing pair conversions, $\gamma Z \to e^- e^+ Z$, with the electron and positron daughters detected in the STAR TPC. Reconstructed photons were used in turn to measure the rate of π^0 production via the $\pi^0 \to \gamma\gamma$ decay channel. This paper discusses the techniques employed and the resulting spectra of photons and π^0s that were measured. A full discussion of all cuts and variables used in this analysis may be found in Ref. [2].

II. DATA ANALYSIS

The data presented in this paper were recorded by the STAR collaboration during the first $\sqrt{s_{NN}} = 130$ GeV Au+Au run at RHIC. Events that had a primary collision vertex position less than 100 and 150 cm distant from the geometric center of the TPC along the beam axis (z-axis) were selected for the photon and π^0 analyses respectively. Details of the STAR geometry are presented in Fig. 1 and discussed in Refs. [14,15]. For the event sample used for π^0 measurements, which were limited by statistical uncertainties, approximately 87% of the events in the minimum bias (least trigger-biased) data set passed the z vertex requirement. With this range of collision vertices, part of the support structure for the silicon vertex tracker (SVT) could be utilized as a converter, as shown in Fig. 1. In addition, the inner field cage and gas (10% CH_4 and 90% Ar) of the STAR TPC were also used as converters. The combined material from both detectors resulted in an average conversion probability of approximately 1% during the data run of year 2000. Although this conversion probability was low, it was compensated by the complete 2π azimuthal acceptance of the STAR TPC.

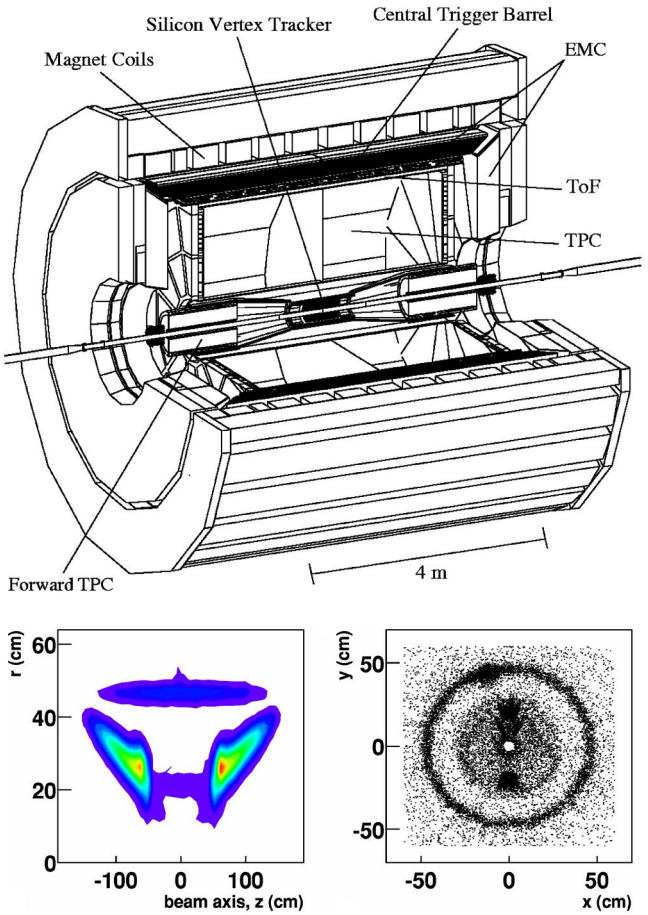

FIG. 1. (Color online) Top figure: layout of the STAR experiment. Lower figures: density profiles of photon conversion points show the layout of the detector material. The structure at $r = 46.5$ cm is the inner field cage of the cylindrical TPC, while below $r = 40$ cm the SVT support cones and material are apparent.

As discussed in Ref. [16], the definition of collision centrality was based on the number of reconstructed primary tracks in the pseudorapidity range $|\eta| < 0.75$. Using this as a basis, four centrality classes were defined, common to both the photon and π^0 analyses. They were an inclusive minimum bias (0%–85% of the total inelastic hadronic cross section), peripheral (34%–85%), midcentral (34%–11%), and central (0%–11%). These centrality classes were selected to allow the extraction of π^0 yield over a wide range of p_t ($0.25 < p_t < 2.5$ GeV/c) in independent regions of centrality. They contained 328 980, 198 196, 87 484 and 449 095 events, respectively.

A. Reconstructing photon pair conversions $\gamma Z \to e^- e^+ Z$

The dominant interaction process for photons with a total energy above 10 MeV is pair conversion, $\gamma Z \to e^- e^+ Z$ (Fig.

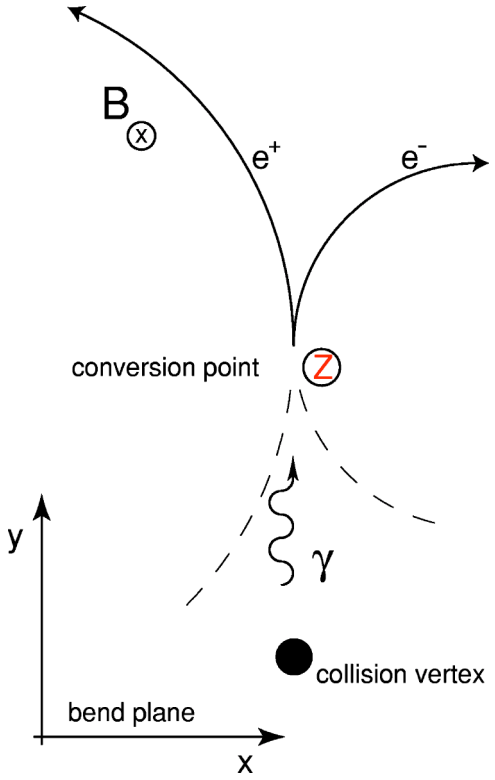

FIG. 2. (Color online) Schematic diagram of $\gamma Z \rightarrow e^- e^+ Z$.

2). Pair conversions that occurred in the detector material before or inside the TPC tracking volume were reconstructed from the resulting charged particle daughters detected in the TPC. This was accomplished in three steps: the selection of track, pair, and primary photon candidates. All three steps utilized the unique topological signature of a photon conversion — two tracks of opposite charge emerging from a secondary vertex with a small opening angle ($\approx m_e c^2/E_\gamma$ radians, where m_e is the electron mass and c is the speed of light).

At the track level, improbable conversion daughters were removed by requiring tracks to satisfy a geometric cut and to have the ionization energy loss expected for an electron in the TPC gas. Neglecting resolution effects, the projection of a daughter track from a primary photon conversion onto the bend plane will form a circle which does not enclose the collision vertex. This is because photons typically propagate some distance before conversion and daughters emerge with a near-zero opening angle (see Fig. 2). Thus, low p_t (<0.3 GeV/c) tracks with circular projections that enclosed the collision vertex in the bend plane of the 0.25 T solenoidal magnetic field were immediately removed (refer to Figs. 3.4 and 4.9 in Ref. [2]). This cut was important, since the elimination of non electron (positron) tracks in this region of p_t via ionization energy loss dE/dx is difficult due to the fact that the highly populated pion band crosses the electron dE/dx band. It was not necessary to use this cut at higher p_t, since the yield of particles drops and electron (positron) identification via dE/dx improves. It is also the case that at higher p_t this cut begins to remove daughters of primary photons since stiff track geometries make the distance

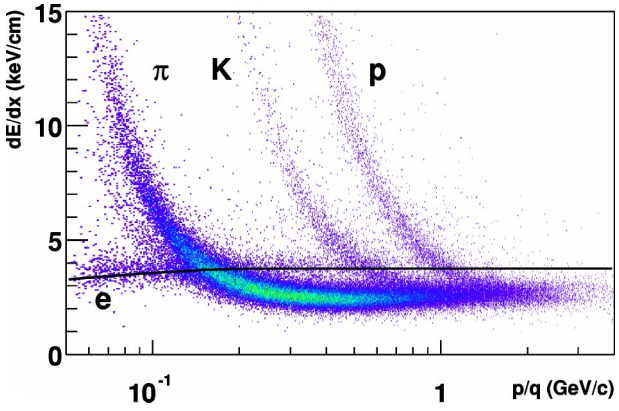

FIG. 3. (Color online) Measured ionization energy loss in the TPC gas dE/dx vs rigidity. The line indicates the predicted dE/dx curve for electrons. Photon selection criteria have not been applied to track candidates in this figure.

from the collision vertex to the closest point on the circular projection of the helix comparable to the resolution of the measurement. At all momenta, electron and positron candidates which had a dE/dx value between -2 and 4 standard deviations ($\sigma_{\rm res}$) of the value expected for electrons and positrons were retained ($\sigma_{\rm res}$ denotes the resolution of charge particle dE/dx measurements in the TPC gas; $\sigma_{\rm res} \approx 8.2\%$ of the dE/dx value measured with a clean sample of electrons and positrons). The predicted energy loss curves for electrons, pions, kaons, and protons are shown as a function of rigidity in Fig. 3. The dE/dx requirement was chosen to be asymmetric, because on the lower side of the electron band other particle bands run in parallel and contamination is more prominent. On the upper side of the electron band other particle bands approach and cross the electron dE/dx band in a narrow range of momentum. This reduced the usefulness of a tight cut on the upper side. It was estimated that approximately 3% of the true photon daughters were removed with this dE/dx requirement.

Photon candidates were found by searching for track pairs which exhibited the topological signature of a photon conversion. Oppositely charged tracks were paired and passed through a geometric filter. The filter required each pair to originate from a secondary vertex with a near-zero opening angle and low invariant mass. Secondary vertices were located by extrapolating daughter candidates to a common point. At the point of closest approach, daughters were required to come within 1 cm of each other in the non-bend plane (rz-plane) and within 1.5 cm of each other in the bend plane (xy-plane), refer to Fig. 4.10 in Ref. [2]. The angular resolutions of opening angle measurements also differed in the two planes. In the non-bend plane and bend plane the precision of opening angle measurements have single Gaussian sigmas near 0.02 and 0.1 radians, respectively. Since even at energies as low as 100 MeV photon conversions on average have an opening angle of 0.01 radians, ten times smaller than the precision in the bend plane, the full opening angle and the opening angle in the non-bend plane of each candidate pair were checked separately. These values were required to be less than 0.4 and 0.03 radians, respectively. The differing angular resolutions in the bend and non-bend

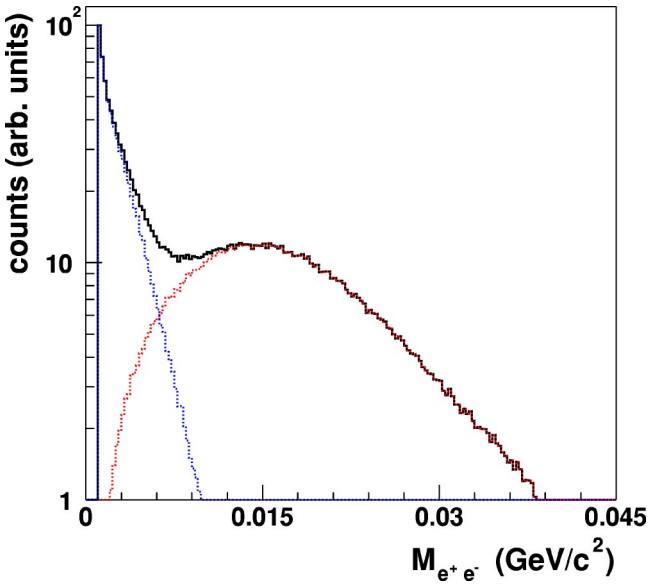

FIG. 4. (Color online) Invariant mass distribution of photon candidates assuming the electron and positron mass for the daughters. The distribution can be separated into two contributions (included with dashed line); a sharp lower-mass peak primarily composed of track-pair geometries that do not overlap in the bend plane, and a higher invariant mass peak from pair geometries that do overlap in the bend plane.

planes are also apparent in the invariant mass distribution of pairs assuming an electron (positron) hypothesis for the daughters (Fig. 4). The invariant mass distribution has a sharp peak near zero and a broad peak close to 0.012 GeV/c^2. The sharp peak at lower mass primarily results from cases where the bend plane projection of the opening angle was assumed to be zero. In these cases, the track geometries do not overlap in the bend plane, so the tracks were assumed to be parallel in the bend plane at the point of closest approach. Track geometries that do overlap in the bend plane lead to a higher invariant mass because the complete opening angle was used in calculation of the invariant mass. In this case, the less precise measure of the opening in the bend plane tends to dominate the result of the invariant mass calculation, moving and smearing the invariant mass peak. For this reason, a cut was placed on the value of the invariant mass of pairs calculated with only the non-bend plane projection of the opening angle. This cut required the invariant mass of candidate pairs to be less than 0.012 GeV/c^2. The minimum mass returned by the calculation is $2m_e$=1.022 MeV/c^2, which is above the first four 0.25 MeV/c^2 wide mass bins in Fig. 4, and causes the absence of entries in the lower mass bins in the figure.

The kinematic parameters for photon candidates were derived from the kinematic variables of the associated daughter tracks. The energy was calculated by summing the electron and positron energies. The angular direction in the bend plane was extracted by forming the crossproduct of the vector from the helix center of the positron to the helix center of the electron, with the magnetic field vector. The angular direction in the non-bend plane was found by averaging the direction of electron and positron at the conversion point. With these three variables all kinematic parameters for photon candidates could be derived.

Primary photon candidates were selected from the set of all photon candidates by requiring the momentum vector to be consistent with the direction of a photon originating from the collision vertex. For these photons, the momentum vector has the same direction as the vector from the collision vertex to the conversion point. The direction of the momentum vector and conversion point vector were compared separately in the bend and non-bend planes, because of the differing angular resolution. For primary photon candidates, the difference between the momentum vector and the conversion point vector was required to be less than 0.035 and 0.015 radians in the bend and non-bend planes, respectively (refer to Fig. 3.9 in Ref. [2]). In order to reduce background in the photon sample from the random pairing of primary tracks, conversion vertices in the region close to the collision vertex ($r_{xy}<10$ cm) were excluded.

B. Photon spectra

Photon spectra were measured as a function of p_t and y in three independent centrality classes as well as for an inclusive minimum bias data set. These spectra were produced from photon candidates identified with the standard event, track, and photon selection criteria (discussed in Sec. II A).

Photon yields were extracted using the particle identification information of the positive daughters in the TPC. A dE/dx deviant variable was constructed by comparing the energy loss predicted as a function of momentum for electrons and positrons with the measured dE/dx and rigidity of daughter candidates, folding in the dE/dx resolution of the TPC. This variable accounts for the momentum dependence in dE/dx, and its value is therefore independent of the daughter particle's momentum and the parent photon's p_t. Consequently, the dE/dx deviant values for daughters of differing momenta could be merged into bins based on the parent photon's p_t and y. Distributions of the dE/dx deviant values of positive daughters were chosen rather than the negative daughter to reduce the number of false photon candidates that arise from knockout electrons which originate when charged particles scatter in the detector material (δ electrons). The remaining contamination from this scattering process, which may result in a knockout electron and positive particle (π,K, or p) having a momentum in a region where the dE/dx bands overlap the positron band (see Fig. 3), was removed by requiring the fraction of the positive daughters energy to the total photon energy to be less than 75%. The shape of the remaining background in the dE/dx deviant distribution was studied on a sample of photon candidates that satisfied anti photon cuts (primarily a sample of background candidates). Anti photon cuts suppress positrons from true photons by requiring the photon selection criteria to be in the outermost extent of the cut distributions. For example, the two-track distance of closest approach for daughter tracks was required to be $1.5<|d_{xy}|<2$ cm and $1.5<|d_z|<1.5$ cm. A two parameter exponential plus linear function was used to describe these background distributions, as shown for one p_t bin in Fig. 5. Parameters of the

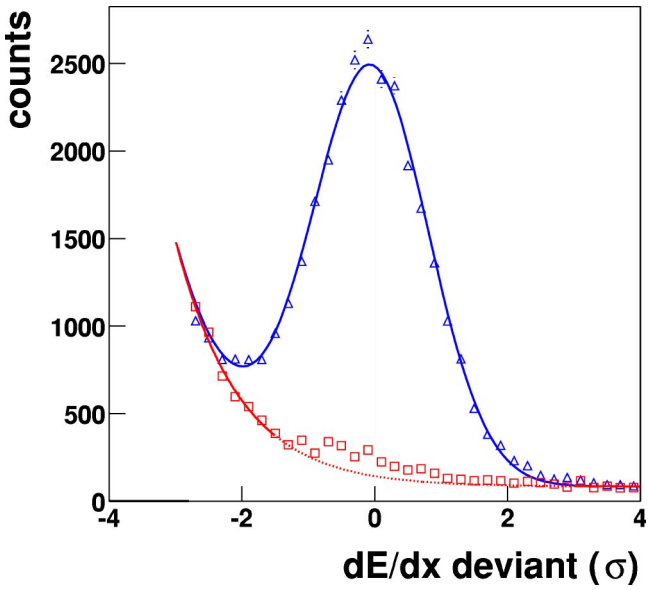

FIG. 5. (Color online) dE/dx deviant distributions of positive daughters with $0.9<p_t<1.05$ GeV/c from photon candidates with $r_{xy}>10$ cm. The distribution of background candidates (boxes and scaled by 1.7) is fit with an exponential plus linear function. The distribution of the positron signal (triangles) is fit with a Gaussian function plus a scaled background function.

background functions were found by fitting to the background distributions with the region around the expected value removed (dE/dx deviants between −1.5 and 3 σ_{res}). This was necessary to avoid fitting the signal from residual photons that still existed after the application of anti photon cuts. With the knowledge of the background shape, the raw yield of photon candidates was extracted using a three parameter Gaussian function plus the background function which had one free scaling parameter (also shown in Fig. 5).

The purity of the photon candidate sample was determined by dividing the integral of the Gaussian function by the integral of the entire Gaussian plus background function between dE/dx deviant values of −2 and 4 σ_{res}. For $p_t<0.75$ GeV/c, the purity of the photon candidate sample is greater than 90% in all centrality classes. In the 0%–11% most central centrality class, where the purity is the lowest, the purity drops linearly from approximately 90% at $p_t=0.75$ GeV/c to about 60% at $p_t=2.4$ GeV/c. A cleaner sample (purity >95% below $p_t=0.90$ GeV/c for the 0%–11% most central collisions) was obtained by requiring photons to convert in the inner field cage and TPC gas, $r_{xy}>40$ cm.

Uncorrected yields were obtained from the weighted sum of the entries in the dE/dx deviant distributions. The weights were extracted by dividing the height of the Gaussian function by the height of the entire fit at the location of each entry. Distributions in y were extracted in a 4×10 array of p_t-y bins to properly account for the variation in efficiency as a function of p_t. Three 0.25 GeV/c wide p_t bins were used below $p_t=0.75$ GeV/c where the efficiency grows rapidly, and one large bin was used for $0.75<p_t<2.5$ GeV/c where the efficiency is flat. The p_t distributions did not require division into p_t and y bins, since the corrected y distributions

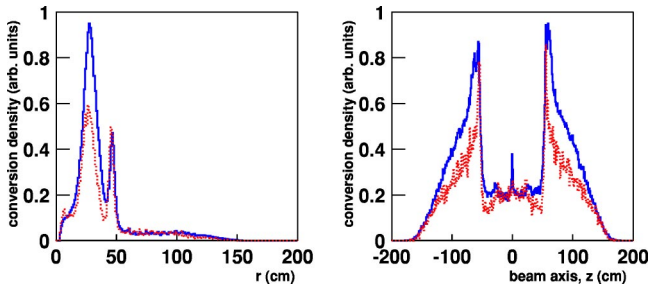

FIG. 6. (Color online) Number of reconstructed photon conversions as a function of the conversion location for both real data (solid line) and GEANT simulated events (dashed line). Left-hand side: conversion density as a function of radial distance from the beam axis. Right-hand side: conversion density as a function of the distance along the beam axis, z.

and the input distributions for the efficiency calculations were both uniform in y for $|y|<0.5$.

Efficiency corrections were applied to each p_t-y bin independently. These corrections were calculated with detailed simulations (GEANT 3.21) of the propagation of photons and daughter particles through a realistic detector geometry. A TPC Response Simulator (TRS) was used to simulate the drift and electronic response of ionization deposited in the TPC. Digital pad signals produced by TRS were embedded pixel-by-pixel into real events.

Each simulated event contained 2000 photons generated flat in p_t and y. On average, approximately 20 of these photons interacted with the detector material (a consequence of the low conversion probability). This added the ionization of about 40 daughter tracks to each real event. This number is less than 2% of the number of charged particles in the embedded phase space in a typical high multiplicity event. Therefore even in high multiplicity events, which are most sensitive to overembedding, the introduction of 2000 photons into each event had a negligible effect on the track reconstruction efficiency. An association process was used to link reconstructed and generated photons. The photon finding efficiencies for different centrality definitions were calculated by dividing the distributions of reconstructed photons correctly associated with a generated photon by the input distributions of generated photons.

To reveal systematic trends caused by differences in the layout of the detector material and the material map used in simulation to calculate efficiency corrections, spectra were produced with different requirements on the minimum distance between the location of conversion and the beam axis in the xy-plane ($r_{xy}>10$ cm and $r_{xy}>40$ cm). It was found that an additional correction factor was needed to compensate for differences in the layouts of the detector material between $r_{xy}=10$ cm and $r_{xy}=40$ cm, as illustrated in Fig. 6. Above $r_{xy}=40$ cm, the material of the inner field cage and the gas of the TPC were well described in the simulation. A correction factor (1.42) was calculated by first normalizing the distribution of conversion density as a function of r_{xy} (Fig. 6) for simulated events to the real data distribution between $r_{xy}=55$ cm and $r_{xy}=100$ cm, then dividing the total number of photon conversions (for all r_{xy}) from real events by the total (normalized) number from simulated events. All

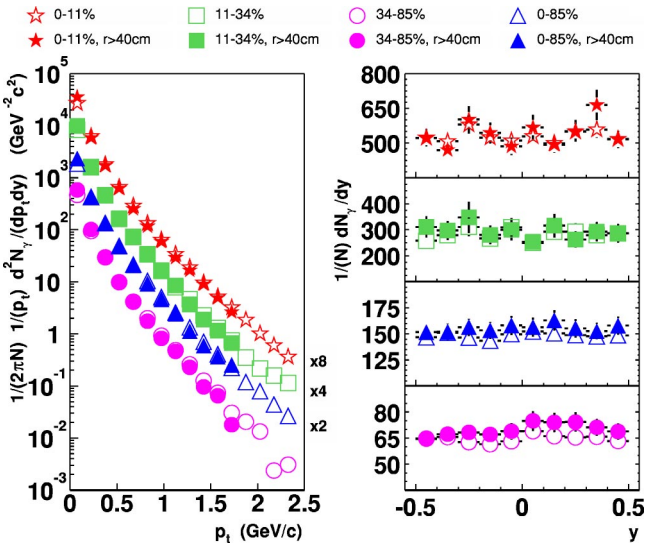

FIG. 7. (Color online) Corrected photon p_t (left-hand side) and y (right-hand side) spectra for ^{197}Au+^{197}Au collisions at $\sqrt{s_{NN}}$ =130 GeV. The p_t distributions are for midrapidity photons, $|y|<0.5$. Statistical uncertainties are shown. Systematic uncertainties in the p_t spectra and on the normalization of the dN/dy spectra have not been included in this figure.

p_t and y data points in the $r_{xy}>10$ cm spectra were linearly scaled by this factor.

Corrected p_t and y spectra for the various centrality classes are shown in Fig. 7. Systematic uncertainties of 7% point-to-point and 12% overall (correlated) have been estimated for the measurements in the p_t spectra. There is a 12% (correlated) systematic uncertainty in the normalization of the y spectra. These uncertainties account for uncertainty in the detection efficiency and potential measurement bias that may arise from differences in the physical and simulated material maps.

Values in the lowest $r_{xy}>10$ cm p_t bins, $0<P_t<0.15$ GeV/c, are systematically 15%–25% lower than in the corresponding $r_{xy}>40$ cm bins. This is attributed to the efficiency correction being underestimated in these bins for the $r_{xy}>10$ cm, because the simulation lacked material between $10<r_{xy}<40$ cm. This gave the inner field cage and TPC gas a larger fraction of the total conversion probability in the simulation, and resulted in a mean r_{xy} conversion point that is closer to the TPC. The combination of the shift in the mean position of conversions and the linear scaling of the spectra, to compensate for differences in the material layouts, artificially increased the efficiency of low p_t photons in the $r_{xy}>10$ cm spectra. Therefore the corrections, which are the inverse of the efficiencies, are too small in the $r_{xy}>10$ cm spectra at low p_t.

C. Measuring the yield of $\pi^0\rightarrow\gamma\gamma$ decays

The uncorrected yield of π^0 mesons was extracted from the invariant mass distributions of photon pairs in various p_t bins. Individual decays could not be uniquely identified, because of the large combinatorial background in the invariant mass distributions. The combinatorial backgrounds were

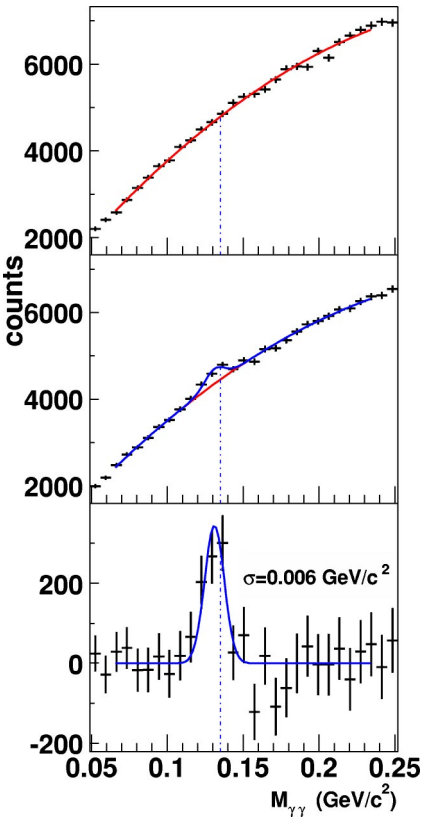

FIG. 8. (Color online) Two-photon invariant mass distributions for candidates with $0.75<p_t<1$ GeV/c in the 0%–11% most central ^{197}Au+^{197}Au collisions at $\sqrt{s_{NN}}$=130 GeV. Top frame: invariant mass distribution with one photon *rotated* by π radians fit with a second order polynomial. Middle frame: invariant mass distribution of photon pairs fit with Eq. (1); the background function is also shown. Bottom frame: invariant mass distribution after the combinatorial background was removed. The enhancement near the π^0 mass is located at 0.131 GeV/c^2 and has a Gaussian sigma of 0.006 GeV/c^2.

simulated by *rotating* the momentum vector of one photon in each pair by π radians in the bend plane. In this way, it was possible to create combinatorial background distributions which preserved event characteristics such as the vertex position along the beam axis, the event multiplicity and anisotropic flow. Due to the azimuthal symmetry of the STAR TPC, this type of rotation also ensured that a consistent geometric acceptance and track reconstruction efficiency were maintained. At the same time these rotations moved and smeared the invariant mass values of the pairs that are correlated through two photon decays. The shape of the resulting background distributions near the π^0 mass (±0.1 GeV/c^2) was well described and smoothed with a second order polynomial (see Fig. 8). This functional form was also used to describe the shape of the combinatorial background in the *unrotated* invariant mass distributions. A Gaussian function was used to describe the enhancement at the π^0 mass. The width (σ) of the enhancement ranged between 4 and 15 MeV/c^2, and was found to be consistent with simulations in all centrality classes and as a function of p_t. This width is a consequence of the photon momentum

resolution, and not the intrinsic mass width of the π^0($\sim$8 eV/c^2). For this reason a Breit-Wigner function that would be appropriate to describe the intrinsic width of such a resonance was not used. Equation (1) is the complete function that was used to describe invariant mass distributions of photon pairs. Systematic uncertainty related to the choice of the invariant mass bin width, δ, was studied by comparing the measured yields for various choices of δ. These studies indicated that the systematic uncertainty due to this effect was much smaller than statistical uncertainties in the measurements.

$$C(x \equiv M_{\gamma\gamma}) = \frac{N\delta}{\sigma\sqrt{2\pi}} e^{-(x-m)^2/(2\sigma^2)} + B(a + bx + cx^2), \quad (1)$$

where δ is the width of the invariant mass bins, N is the number in the Gaussian peak, and B is the scale factor of the background function.

A feature of this method of photon reconstruction is that the location of the enhancement from π^0 decays in the two-photon invariant mass distribution is a few MeV/c^2 lower than expected (see Fig. 8). This is attributed to energy loss experienced by the electrons and positrons in the detector material. The "global" tracking routine used in this analysis only compensated for energy loss in the TPC gas and not for that in other detector material. This resulted in the reconstructed momentum for electrons and positrons originating prior to the gas volume of the TPC to be systematically lower than their original momentum. The small ($\sim$1 MeV on average) energy loss experienced by each of the four daughter particles translated to a few MeV/c^2 shifts in the location of the π^0 invariant mass peak. This hypothesis is consistent with a similar feature in simulated events. The location of the reconstructed invariant mass peak for simulated π^0s systematically decreased as the radial distance between the beam axis and conversion point of the closer photon in the pair decreased. This implies that a larger π^0 mass deviation occurs when more detector material is between the conversion point and the TPC. The reconstructed energy of simulated photons was also systematically lower than the energy input to the simulation and larger deviations also occurred when more detector material was between the conversion point and the TPC.

D. Spectra of π^0 mesons

Two iterations (described in Sec. II C) were performed to fit the data and extract the yield of π^0s as a function of p_t. For the first iteration, four free parameters were used in the fit: the yield (N), mass (m), and width (σ) of the Gaussian function describing the peak, and the scale factor for the background function (B). For the second iteration it was assumed that the width of the invariant mass peak increased linearly with p_t, as seen in the simulated events. The width parameters for the fits in the second iteration were obtained from a linear fit to the widths found in the first iteration. The values of the slopes for these linear fits [$\approx$3(MeV/c^2)/(GeV/c)] were consistent with those found in simulation. The width parameters were then fixed to the value of the linear function at the center of each p_t bin. This reduced the number of free parameters in the second pass to three and increased the stability of the fits.

Uncorrected yields about midrapidity ($|y|<1$) were extracted in various p_t bins for the four different centrality classes. The narrow 6 MeV/c^2 width (sigma) of the enhancement at the π^0 mass measured with this reconstruction method is significantly better than what is typically achieved using a conventional lead-scintillator sampling calorimeter (20 MeV/c^2 sigma). The improvement is a result of the excellent photon energy resolution (3% at 1 GeV) obtained with this method of photon reconstruction. The narrow width improves the signal to background ratio and enables the extraction of raw π^0 yields at low p_t($p_t<0.75$ GeV/c) where the signal to background ratio is seriously degraded by a large combinatorial background.

Efficiency corrections were calculated with a procedure similar to the one used to calculate the photon detection efficiencies (described in Sec. II B), except that π^0 were selected in GEANT. Only the ionization in the TPC gas from daughters of those π^0 selected in GEANT was passed to TRS. This was necessary to perform the calculation in a reasonable amount of cpu time and to prevent saturating real events with ionization. One consequence of the low conversion probability is that on average only 1 in 10 000 $\pi^0 \to \gamma\gamma$ decays is expected to be detected through the reconstruction of pair conversions. At the same time about 1 in 50 $\pi^0 \to \gamma\gamma$ decays produces a photon that converts to create a pair of tracks that ionize the gas in the TPC. Selecting detectable $\pi^0 \to \gamma\gamma$ decays in GEANT (π^0s that decay into two photons, with both photons undergoing interactions which create at least one daughter within the TPC acceptance) reduced the amount of uninteresting ionization in each simulated event. With this selection, the insertion of up to 12 detectable $\pi^0 \to \gamma\gamma$ decays into each event added less than 2% to the number of tracks in the phase space of the embedding. These events were reconstructed with the same software used to reconstruct real events. Reconstructed photons that could be associated with a photon from a simulated $\pi^0 \to \gamma\gamma$ decay were retained. These photons were used to generate two-photon invariant mass distributions. The yields of simulated π^0s were calculated in the same p_t and centrality bins, and with the same fitting procedure as the raw yields. Efficiency corrections for these bins were obtained by dividing the reconstructed distributions by the input distributions.

Corrected p_t spectra of π^0s were obtained by applying efficiency corrections to the p_t distributions of the raw yields. The corrected spectra are shown in Fig. 9. The uncertainties shown are statistical and mainly reflect the low number of real π^0s measured. They combine the uncertainty in the raw yields and efficiency corrections. Systematic uncertainties due to the cuts used were studied by varying track, photon, and π^0 cuts. These studies revealed that the statistical fluctuations dominate the systematic variations in this analysis.

Corrections to the normalization of the spectra were made to compensate for the overall difference in the photon conversion probability in the real detector material and that used in simulation. These correction factors were based on the corrected yield of π^0s ($Y_{r_{xy}>40}$) for photons that converted in the inner field cage or the TPC gas ($r_{xy}>40$ cm) where the two material maps are consistent with each other (see Fig. 6).

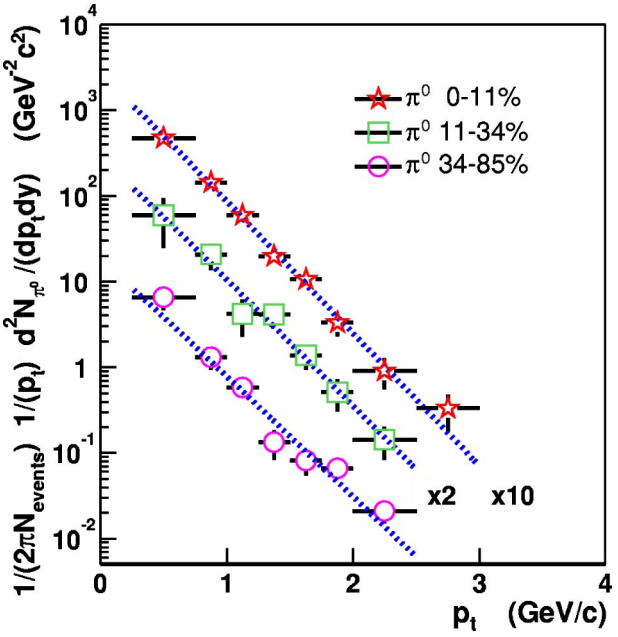

FIG. 9. (Color online) Transverse momentum spectra of the π^0 meson about midrapidity, $|y|<1$, for different centrality bins. Along with the point-to-point statistical uncertainties shown, the spectra have a common uncertainty in the normalization of ±40%. The central data (0%–11%) has an additional normalization uncertainty of ±19%, which results in a total normalization uncertainty of ±49%. Dashed lines indicate Boltzmann fits to the spectra.

For $1<p_t<2$ GeV/c, a centrality-independent material correction factor was directly extracted by dividing $Y^{\min}_{r_{xy}>40}$ by $Y^{\min}$ for minimum bias events. In this p_t interval, the ratio of the π^0 efficiency for $Y^{\min}_{r_{xy}>40}$ to the efficiency for $Y^{\min}$ is uniform. Therefore, it was not necessary to correct this factor for interplay between the shape of the efficiency correction and the exponentially falling spectrum. This material correction factor was crosschecked in three different p_t windows. The resulting systematic variation in these factors was found to be 5× smaller than the statistical uncertainty in an individual factor (~40%). The large statistical uncertainty is a consequence of the relatively small number (~50) of π^0s reconstructed from photons with $r_{xy}>40$ cm. The systematic uncertainty associated with the choice of the invariant mass bin width was also found to be much smaller than the statistical uncertainty. The material correction factor for the minimum bias data set was 0.31 ± 0.12, with $1<p_t<2$ GeV/c as the window of π^0 p_t. This factor was used to scale the normalization of centrality classes formed by taking subsets of the minimum bias triggered data set (0%–85%, 34%–85%, and 34%–11%). The uncertainty in this factor (±0.12 or 40%) is common for all these centrality bins and cancels out when ratios are taken. This factor can not be used to normalize the 0%–11% centrality bin, because of the differing z vertex distributions between the central and minimum bias triggered data sets. A separate centrality-independent factor was calculated for $|z_{\text{vertex}}|<75$ cm where the vertex distributions are similar in the two data sets. Minimum bias triggered events with z vertices in this region were used to calculate the factor. The factor, 0.26 ± 0.11, was obtained by dividing $Y^{\min}_{r_{xy}>40}$ by $Y^{\min}_{|z_{ver}|<75}$. Using this factor, the normalized yield for the 0%–11% centrality bin was computed by taking the product of the factor and $Y^{\text{cent}}_{|z_{ver}|<75}$. This normalized yield, $Y^{\text{cent}}=12.0\pm5.7$ for $1<p_t<$GeV/c, is independent of the vertex distribution. The final 0%–11% spectrum was scaled by $Y^{\text{cent}}/Y^{\text{cent}}_{|z_{ver}|<150}=0.27\pm0.14$. In summary, the 0%–11% most central class of events has the same common uncertainty of ±40% plus an additional uncertainty of ±19%. These two uncertainties were combined (±49%) for the purpose of comparison to other spectra, like the spectrum of charged hadrons.

III. CONTRIBUTION OF THE $\pi^0\rightarrow\gamma\gamma$ DECAY TO THE INCLUSIVE PHOTON SPECTRUM

Electromagnetic decays of neutral mesons are the dominant source photons in heavy ion collisions. Among these, the $\pi^0\rightarrow\gamma\gamma$ decay is the largest contributor to the spectrum of inclusive photons. Its large contribution hides the signal from other sources, such as direct photons emitted during the early stages of heavy ion collisions.

To investigate how the $\pi^0\rightarrow\gamma\gamma$ decay contributes to the inclusive photon spectrum, the p_t distributions of π^0s were used to generate the single photon spectrum expected for the daughters of $\pi^0\rightarrow\gamma\gamma$ decays. The p_t distributions of π^0 were fit with both a Boltzmann function and a Bose-Einstein function. For both functions, the total energy of the π^0 was replaced by its transverse energy ($\sqrt{p_t^2c^2+m_\pi^2c^4}$) under the assumption that the system is boost invariant near midrapidity. This assumption is supported by the flat shape of particle rapidity distributions close to midrapidity [17,18]. Other more sophisticated functions, incorporating resonances that decay into π^0s and/or handling radial expansion of the system in more detail with additional parameters, were not chosen because the additional parameters were not well constrained by the seven or eight data points of the spectra. Both the Boltzmann and Bose-Einstein functions treat the system as a thermalized gas and converge to exponential functions at high p_t.

Distributions of the p_t dependence of π^0s were generated using these functions, assuming that the rapidity and azimuthal distributions are flat. The input rapidity distribution of π^0s was limited to $|y|<2$. This rapidity window produces more than 99% of the photons with $|y|<0.5$ from $\pi^0\rightarrow\gamma\gamma$ decays. These distributions were passed through a Monte Carlo decay simulator used to calculate the $\pi^0\rightarrow\gamma\gamma$ decay kinematics and boost between the center of momentum and laboratory frames. The momentum information of the decay photons was used to produce the single photon p_t spectra of the daughters.

The fraction of the photons from $\pi^0\rightarrow\gamma\gamma$ decays in the inclusive photon spectra was calculated as a function of p_t by dividing the simulated spectra by the measured inclusive photon spectra, as shown in Fig. 10. The shape of the resulting distributions for various centrality classes is independent of the uncertainty in the normalizations of the π^0 spectra, but may depend on the assumed p_t dependence of the π^0 spectra. For this reason, the fractions are shown for $p_t>0.45$ GeV/c,

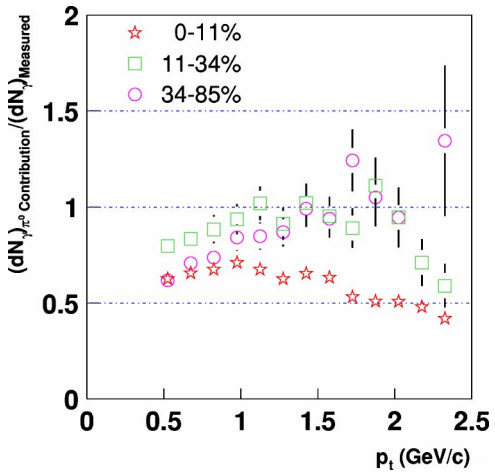

FIG. 10. (Color online) The ratio as a function of p_t of the distributions of photons from $\pi^0 \rightarrow \gamma\gamma$ decays to the measured photon spectra. The $\pi^0 \rightarrow \gamma\gamma$ photon distributions were generated assuming that the p_t dependence of the π^0 p_t spectra follow a Boltzmann distribution. These ratios include both statistical and systematic uncertainties in the photon spectra. Uncertainties in the normalization of the π^0 spectra arise as p_t independent uncertainties and have not been included. Normalization uncertainties in the π^0 spectra are 40%, correlated between all ratios, with an additional 19% uncorrelated uncertainty for the 0%–11% centrality ratio. Uncorrelated p_t dependent uncertainties that arise from the uncertainty in the slope parameters of fits to the π^0 p_t spectra (11%, 9%, and 5%, respectively for the 34%–85%, 11%–34%, and 0%–11% centrality classes) have not been included.

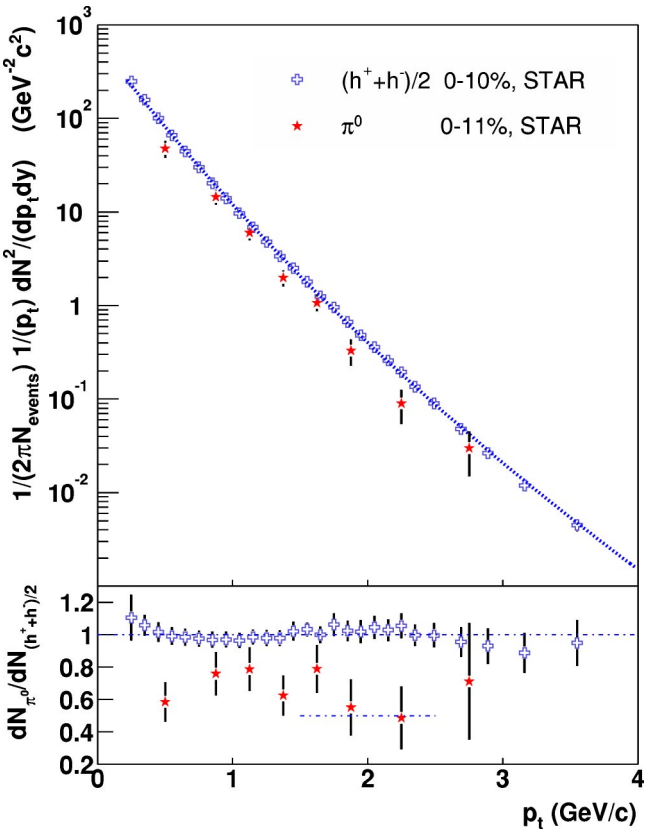

FIG. 11. (Color online) Top frame: comparison between STAR π^0 and inclusive charged hadron $[(h^- + h^+)/2]$ spectrum [20] about midrapidity for ^{197}Au+^{197}Au collisions at $\sqrt{s_{NN}}$=130 GeV. Bottom frame: ratios of these spectra to a power law fit to the STAR inclusive charged hadron spectra. For reference, dashed lines indicate $dN/dN_{(h^- + h^+)/2\ fit}$ of 0.5±0.25 and 1. Normalization uncertainties in both the π^0(±49%) and inclusive charged hadron (±11%) measurements have not been included with the data points.

where the photon contribution is determined from π^0s in and above the measured p_t interval. The kinematics of $\pi^0 \rightarrow \gamma\gamma$ decay limit the p_t of the daughter photons. For example, a π^0 of $p_t < 0.435$ GeV/c can only produce photons with $p_t < 0.45$ GeV/c . Thus, the unmeasured portion of the π^0 spectra below p_t=0.25 GeV/c does not contribute to the photon spectra in the region where the fractions are plotted.

The fraction of photons from $\pi^0 \rightarrow \gamma\gamma$ decays in the inclusive photon spectrum is approximately constant between $0.75 < p_t < 1.65$ GeV/c. For the 0%–11% most central event class, the fraction begins to decrease substantially near p_t=1.65 GeV/c assuming either the Boltzmann function or Bose-Einstein function to describe the p_t spectra of π^0s. Specifically, the relative contribution from $\pi^0 \rightarrow \gamma\gamma$ decays decreases by 20%±5% from p_t=1.65 GeV/c to p_t =2.4 GeV/c. Both point-to-point uncertainties in the photon spectrum as well as substantial uncertainty in the slope parameters of the Boltzmann (0.281 GeV±0.013) and Bose-Einstein (0.289 GeV±0.014) fits have been included in the 5% uncertainty in the region of the decrease. A similar trend was observed by the WA98 collaboration in ^{208}Pb+^{208}Pb collisions at $\sqrt{s_{NN}}$=17.2 GeV [5]. The WA98 collaboration reported an excess of photons above 1.5 GeV/c in central collisions after accounting for photons from all expected electromagnetic decays. For electromagnetic decays other than the $\pi^0 \rightarrow \gamma\gamma$ decay, the $\eta \rightarrow \gamma\gamma$ decay channel is expected to be the next largest contributor. From p^t=1 GeV/c to p_t=4 GeV/c, its contribution is expected to be approximately 15% and to be fairly uniform in p_t, increasing less than 5% per GeV/c. The WA98 collaboration has estimated that the summed contribution of all other electromagnetic decays is less than a few percent at SPS energies. Based on the above assumptions (the π^0 p_t spectrum has a Boltzmann or Bose-Einstein p_t dependence, the η contribution increases by less than 5% per GeV/c, and the summed contribution of all other electromagnetic decays is less than a few percent) it is unlikely that electromagnetic decays fully account for the observed single photon yields in the 0%–11% most central event class.

IV. COMPARISONS TO PUBLISHED DATA

Comparisons between the 0% and 11% π^0 spectrum and the 0 and–10% charged hadron spectrum were used to study the composition of the hadron spectrum as a function of p_t. The ratio of the π^0 data points to a power law function fit to the charged hadron spectrum $[(h^- + h^+)/2]$ is shown in Fig. 11. At p_t=2 GeV/c the ratio of π^0s to charged hadrons approaches 50% (also shown in Fig. 11). Assuming isospin symmetry for charged and neutral pions $[(dN_{\pi^+} + dN_{\pi^-}) \equiv 2(dN_{\pi^0})]$ the proton to pion ratio is close to 1 at p_t

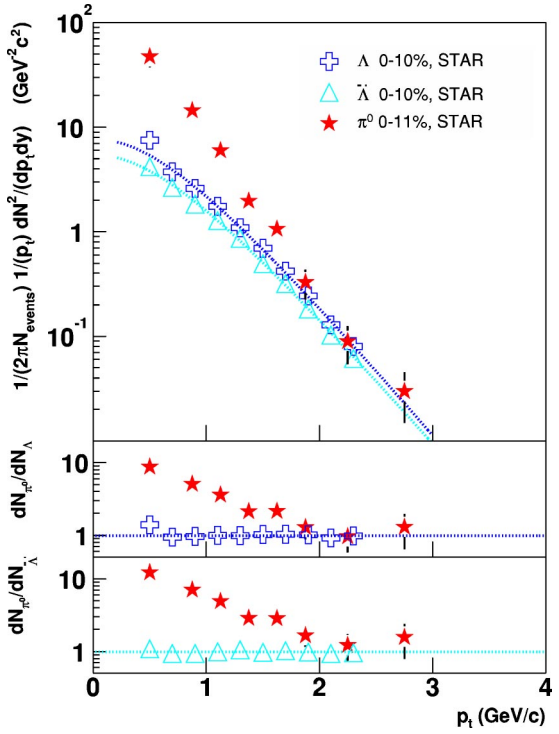

FIG. 12. (Color online) Top frame: comparison between STAR π^0, and $\Lambda(\bar{\Lambda})$ measurements about midrapidity for ^{197}Au+^{197}Au collisions at $\sqrt{s_{NN}}=130$ GeV . Lower frames: ratios of these spectra to Bose–Einstein function fits to the STAR Λ and $\bar{\Lambda}$ measurements. For reference, dashed lines indicate $dN/dN_{\Lambda(\bar{\Lambda})\text{fit}}$ of 1. Normalization uncertainties in both the π^0 (±49%) and $\Lambda(\bar{\Lambda})$(±10%) measurements have not been included with the data points.

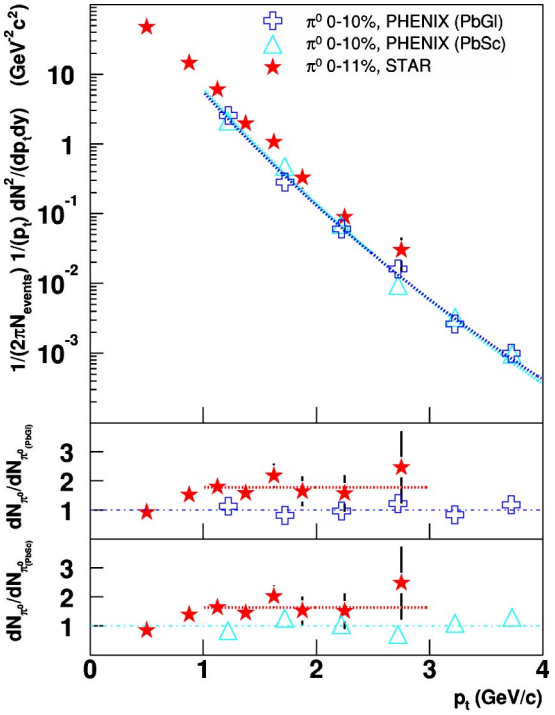

FIG. 13. (Color online) Top frame: comparisons between the STAR π^0 measurement and PHENIX π^0 measurements [21] about midrapidity for ^{197}Au+^{197}Au collisions at $\sqrt{s_{NN}}=130$ GeV. Lower frames: ratios of these spectra to a power law fit to the PHENIX π^0 measurements. For reference, dashed lines in the lower frames indicate $dN/dN_{\text{PHENIX}\pi^0\text{fit}}$ of 1, and 1.78±0.98 and 1.64±0.86 in the middle and bottom frames respectively. Normalization uncertainties in both the STAR (±49%) and PHENIX (±25% for PbGl and ±20% for PbSc) π^0 measurements have not been included with the data points.

=2 GeV/c. This result is similar to the previous observation in central collisions that the "$\bar{p}$ and p yields are comparable to the $\pi^{+/-}$ yields" [19]. Another method of probing the ratio of baryons to mesons in the system is by examining the ratio of π^0 to Λ production (shown in Fig. 12). In this figure, Bose-Einstein functions have been used to describe the Λ and $\bar{\Lambda}$ spectra. The value of the π^0 data points has been divided by the value of the Bose-Einstein function describing the Λ and $\bar{\Lambda}$ spectra at the center of the bins to obtain the π^0–Λ, and π^0–$\bar{\Lambda}$ ratios. At $p_t=2$ GeV/c these ratios are approximately 1, consistent with other measurements of the baryon to meson ratio.

A comparison of the π^0 spectrum for the 0%–11% centrality class was also made to other identified pion spectra for central collisions at $\sqrt{s_{NN}}=130$ GeV. The PHENIX experiment has published π^0, π^+, and π^- spectra for central events [19,21]. The π^0 spectra were measured via the $\pi^0\rightarrow\gamma\gamma$ decay channel using both lead-scintillator (PbSc) and lead-glass (PbGl) calorimeters. These data overlap the STAR π^0 measurement in the range $1<p_t<3$ GeV/c. Ratios between the central STAR π^0 spectrum to power-law fits of the PHENIX π^0 spectra indicate that the shapes of the spectra are consistent (Fig. 13) although the two experiments have a systematic offset in normalization. In the region of overlap, the STAR π^0 spectrum is systematically higher than the PHENIX spectra. A systematic difference in the same direction is also observed in comparisons between the charged hadron spectra $[(h^++h^-)/2]$ from the two experiments for $1<p_t<3$ GeV/c. Direct comparison of the 0%–11% STAR π^0 spectrum and the 0%–5% PHENIX $\pi^\pm$ spectrum shows the two are consistent in shape (Fig. 14), although once again the normalizations are systematically different once a linear scale factor (0.91±0.04, deduced from C values given in [20]) is applied to convert the 0%–5% $\pi^\pm$ data to the 0%–10% centrality class. These ratios indicate that meson to baryon ratios are *internally* consistent within PHENIX and STAR, although between PHENIX and STAR the normalization of the spectra is systematically shifted for p_t between and 3 GeV/c.

V. CONCLUSION

We have presented the first inclusive midrapidity, $|y|<0.5$, photon spectra as a function of centrality from ^{197}Au+^{197}Au collisions at $\sqrt{s_{NN}}=130$ GeV. The spectra of π^0s about midrapidity, $|y|<1.0$, have been presented; as well as the contribution from $\pi^0\rightarrow\gamma\gamma$ decays to the inclusive photon spectrum. Near $p_t=1.65$ GeV/c the fractional contribution from $\pi^0\rightarrow\gamma\gamma$ decays to the inclusive photon spec-

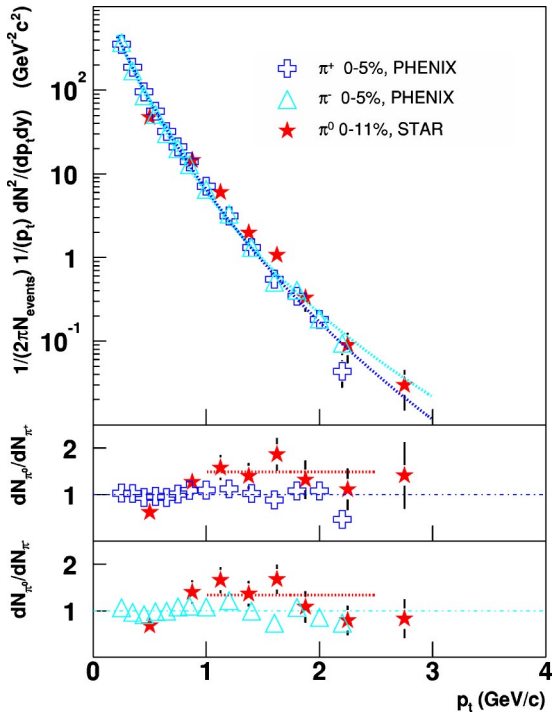

FIG. 14. (Color online) Top frame: comparison between the STAR π^0 measurement and PHENIX charged pion measurements [19] about midrapidity for ^{197}Au+^{197}Au collisions at $\sqrt{s_{NN}}$ =130 GeV. Lower frames: ratios of these spectra to a power law fit to the PHENIX charged pion measurements. For reference, dashed lines in the lower frames indicate $dN/dN_{PHENIX\ \pi^0\mathrm{fit}}$ of 1, and 1.49±0.75 and 1.34±0.67 in the middle and bottom frames, respectively. Normalization uncertainties in both the π^0 (±49%) and charged pion (±11% measurements have not been included with the data points.

trum for the 0%–11% most central collisions begin to decrease significantly. This decrease indicates that relative to the $\pi^0 \rightarrow \gamma\gamma$ decay, the contribution from other sources of photons increases with p_t. In order to understand the origin of this decrease other electromagnetic decays must be measured or estimated. The combination of increased event statistics in future measurements with the excellent energy resolution achieved using this photon detection technique ($\Delta E/E \approx 2\%$ at 0.5 GeV/c) will make the measurement of the η feasible. A statistically significant enhancement in the two-photon invariant mass distribution has already been observed in the vicinity of the η mass. Increased event statistics will also lead to higher precision measurements and extend the p_t range of the π^0 spectra. Advances in these directions will not only enhance our understanding of contributions to the single photon spectra, but will also aid measurements of the relative abundance of mesons and baryons at high p_t ($>$3 GeV/c) where the expected effects of collective motion become less dominant.

ACKNOWLEDGMENTS

The authors thank the RHIC Operations Group and RCF at BNL, and the NERSC Center at LBNL for their support. This work was supported in part by the HENP Divisions of the Office of Science of the U.S. DOE; the U.S. NSF; the BMBF of Germany; IN2P3, RA, RPL, and EMN of France; EPSRC of the United Kingdom; FAPESP of Brazil; the Russian Ministry of Science and Technology; the Ministry of Education and the NNSFC of China; Grant Agency of the Czech Republic, FOM and UU of the Netherlands, DAE, DST, and CSIR of the Government of India; the Swiss NSF.

[1] E. V. Shuryak, Sov. J. Nucl. Phys. **28**, 408 (1978).
[2] I. J. Johnson, Ph.D thesis, University of California, Davis, 2002, LBNL Report No. LBNL-51506.
[3] J. I. Kapusta and S. M. H. Wong, *Proceedings of the XXIX ISMD'99* (World Scientific, Singapore, 1999), p. 346; hep-ph/9909573.
[4] T. Peitzmann and M. H. Thoma, Phys. Rep. **364**, 175 (2002).
[5] M. M. Aggarwal *et al.*, Phys. Rev. Lett. **85**, 3595 (2000).
[6] J. Kapusta, P. Lichard, and D. Seibert, Phys. Rev. D **44**, 2774 (1991).
[7] E. Shuryak and L. Xiong, Phys. Rev. Lett. **70**, 2241 (1993).
[8] D. K. Srivastava and K. Geiger, Phys. Rev. C **58**, 1734 (1998).
[9] L. Xiong, E. Shuryak, and G. E. Brown, Phys. Rev. D **46**, 3798 (1992).
[10] J. Cleymans, K. Redlich, and D. K. Srivastava, Phys. Rev. C **55**, 1431 (1997).
[11] P. Aurenche *et al.*, Phys. Rev. D **58**, 085003 (1998).
[12] D. K. Srivastava, Eur. Phys. J. C **10**, 487 (1999).
[13] J.-e Alam *et al.*, Phys. Rev. C **67**, 054902 (2003).
[14] M. Anderson *et al.*, Nucl. Instrum. Methods Phys. Res. A **499**, 659 (2003).
[15] H. S. Matis *et al.*, Nucl. Instrum. Methods Phys. Res. A **499**, 802 (2003).
[16] K. H. Ackermann *et al.*, Phys. Rev. Lett. **86**, 402 (2001).
[17] C. Adler *et al.*, Phys. Rev. Lett. **87**, 112303 (2001).
[18] B. B. Back *et al.*, Phys. Rev. Lett. **87**, 102303 (2001).
[19] K. Adcox *et al.*, Phys. Rev. Lett. **88**, 242301 (2002).
[20] K. Adcox *et al.*, Phys. Rev. Lett. **88**, 022301 (2001).
[21] C. Adler *et al.*, Phys. Rev. Lett. **89**, 202301 (2002).